HENRY GRANJON PRIZE COMPETITION 2006
Winner, Category D
"Human related subjects"
METHOD FOR SAMPLING AND CHARACTERIZING ARC WELDING FUME PARTICLES

J.W. Sowards

The Ohio State University, Columbus (United States)

ABSTRACT

Arc welding fume may pose a serious risk to the health and safety of welders and operators in the welding industry. Many methods have been employed to collect and characterize welding fume in the past but previous studies have often not used a combination of techniques that give the full picture on the nature of welding fume. This study was employed to collect fume generated by a variety of arc welding processes, including shielded metal arc welding (SMAW: E6010, E7018, E308-16) and gas metal arc welding (GMAW: ER70S-6 with 100 % CO_2 and 75 % Ar-25 % CO_2 shielding gases), and to characterize the fume by size distribution, chemical composition, structure, and morphology with state-of-the-art techniques. This requires the use of multiple imaging and analysis techniques since the size variation of welding fume particles is quite large. Collection of welding fume generated by a variety of common electrodes was performed with an electrical low-pressure cascade impactor (ELPI) to size particles by their aerodynamic diameters and develop particle size distributions. A fume collection hood was also used to collect bulk fume samples and measure fume generation rates. Fume particles on the impactor stages were imaged using high resolution scanning electron microscopy (HR-SEM) and high resolution transmission electron microscopy (HR-TEM), revealing the presence of three fume particle morphologies including spherical, agglomerated, and irregular. TEM revealed the presence of a core-shell particle structure. Chemical analysis and phase identification was also performed for individual particles and bulk stages with energy dispersive X-ray spectroscopy (SEM-XEDS and TEM-XEDS), X-ray diffraction (XRD), and X-ray photoelectron spectroscopy (XPS). Bulk fume and individual particles analyzed were largely metal-oxides with a Fe_3O_4-type crystal structure. Using these advanced characterization techniques in conjunction with one another provides an overall picture of fume that has been previously unattainable.

IIW-Thesaurus keywords: *Sampling; Fume analysis; Analysis techniques; Chemical analysis; Fume; Health and safety; Occupational health; Toxic materials; Size; Dimensions; Particles; Shape; Composition; Measurement; Practical investigations; Electron microscopes; Measuring instruments; Microscopes; FCA welding; Arc welding; GMA welding; Gas shielded arc welding; MMA welding; Reference lists.*

1 INTRODUCTION

Collection and characterization of individual and bulk welding fume particles is highly important for understanding the possible impact of fume on the occupational health of those working in areas related to metal joining. Fumes are one of the unwanted byproducts of the various arc welding processes and have encouraged extensive studies over the past 50 years, as speculation has increased of medical problems arising from overexposure to fume during welding. According to the American Welding Society, "Overexposure is exposure that is hazardous to health and exceeds the permissible limits specified by govern-

Doc. IIW-1751-06 (ex-doc. VIII-2018-06) recommended for publication by Commission VIII "Health and Safety".

ment agencies such as the U.S. Department of Labor, Occupational Safety and Health Administration (OSHA), Regulations 29 CFR 1910.1000, or other recognized authority, such as the American Conference of Governmental Industrial Hygienists (ACGIH) in its publication *Threshold Limit Values for Chemical Substances* and *Physical Agents in the Workroom Environment*' [1]. The permissible threshold levels of potentially harmful elements typically found in welding fume, such as Cr, Mn, and Ni, are constantly decreasing [2]. For this reason, it is important to be able to approximate the levels of fume and their compositions in a typical welding environment since these fumes may eventually be inhaled by welding personnel in these settings.

A welding fume characterization study must be multidisciplinary, drawing upon welding physics, aerosol science, and materials science and chemistry. Knowledge of welding arc physics is necessary to understand the basics of fume formation. Aerosol science provides the necessary means to collect and understand the mobility of welding fume in a welding production setting. Lastly, materials science and chemistry provide a method to analyze the composition and structure of the fume after it has been collected. The epidemiological effects of fume on welders are also an important issue which must be considered, but is beyond the scope of the present study.

Welding fume formation occurs by different mechanisms. The intense heat of a welding arc causes vaporization of the electrode rod (and flux in processes such as SMAW and FCAW). The smallest particles (diameters < 100 nm) are formed by vaporization and homogenous nucleation of particles from the vapour phase [3, 4]. Accumulation occurs as primary particles experience further growth due to collisions with other primary particles as well as particle agglomerates. If the colliding particles are liquid, they will form a single sphere. If the collisions are between solid particles they may be held together by van der Walls bonding, electrostatic or magnetic forces, or they may sinter. Since welding fumes are generally formed by vaporization of alloys and possibly a flux, multiple elements are present in the vapour. These elements will have different vapour pressures resulting in condensation of elements with the highest vapour pressures on the surface of previously nucleated particles, resulting in the formation of core-shell particles. Since the different fume formation mechanisms result in variations in particle size and composition [5], a variety of analytical techniques are required for characterization as discussed later.

The general terminology used to describe size ranges of aerosol particles divides sizes into three ranges: coarse, fine, and ultra-fine [6]. Ultra-fine particles are those particles with a diameter less than 0.1 µm (< 100 nanometers). Fine particles fall in the range between 0.1 µm and 2.5 µm (100 – 2 500 nanometers), and coarse particles are considered to be particles greater than 2.5 µm (> 2 500 nanometers) in diameter. Fume particles in the respirable range are considered to be less than 10 µm in diameter [7]. There are some discrepancies about which size ranges will be deposited in the lungs and exhaled. Friedlander asserts that particles in the range of 0.1 – 1.0 µm will be inhaled and then exhaled, while the finer particles (below 100 nanometers) will be deposited in the lungs and furthermore dissolved into the blood stream [8]. It has been debated that the majority of particles below 100 nanometers are even possibly exhaled [9]. Although the respirable particle size ranges are important to consider, only the aerosol particle size ranges (coarse, fine, ultrafine) are used in the present study.

Aerodynamic (equivalent) particle diameter is an important concept to consider since particles have different morphologies that cause them to behave differently in a stream of air [10]. These morphologies include varying geometry, density, and size. Unless all particles in a given study are spherical in geometry, it becomes difficult to apply the geometric term "diameter" to those particles. Particles may also consist of different elements or compounds, which would therefore change the density of the particles. Therefore it becomes necessary to define a way to compare particles of all shapes and densities. Aerodynamic diameter is used to relate the effective diameters of particles with varying morphologies and is defined as the diameter of a spherical particle with a density of 1 gm/cm^3 with the same aerodynamic (or inertial) properties in the gas as the particle of interest [10]. Cascade impactors, such as the one used in this study, utilize the principle of particle inertia and aerodynamic diameter to separate particles. This is discussed in greater detail later. This principle is also applicable to respiration of particles since particle inertia governs how deep particles will penetrate into the lungs [8].

Imaging of the larger particle sizes is most suited to scanning electron microscopy (SEM) since it can achieve a broad range of magnifications and has good depth of field, making it suitable for examining particle morphology. This technique can show details on the order of tens of nanometers, when in high resolution (HR-SEM) mode, making it the most suitable imaging technique for any particle greater than about a hundred nanometers in diameter (coarse and fine particle sizes). When combined with XEDS, SEM can be a useful technique to analyze single particle compositions as well as bulk fume samples. This technique can provide an excellent sample survey before other techniques are performed since it is quite simple to analyze morphology and chemical composition of many particles in one session of using the instrument. A drawback to SEM-XEDS is that atomic numbers lower than Na (z = 11) are difficult to quantify [5, 11]. XEDS as a chemical analysis technique is semi-quantitative at best due to low atomic number quantification problems and large beam-particle interaction volumes which can generate X-ray signals from multiple particles.

A suitable imaging technique for particles below 300 nanometers is transmission electron microscopy (TEM). This technique is common to analysis of many types of aerosol since it can image these particles better than other methods, providing insight into morphology of ultra-fine particles [12]. Normally, metallurgical samples would have to be sectioned into thin foil sam-

ples so that the TEM electron beam can easily pass through the sample. However, many of the fume particles produced by welding are of such small diameters, the electron beam passes easily through them. X-ray microanalysis can be performed in TEM by utilizing XEDS. Using this technique in the past, compositions of particles only several nanometers in diameter have been analyzed [5, 12, 13] and particle in-homogeneity has been observed [4, 9, 14]. Selected area diffraction (SAD) and high resolution (HR-) TEM may be used to examine the structure of these small particles if they are crystalline in nature.

Welding fume is essentially a poly-crystalline powder that is easily analyzed with an X-ray powder diffractometer [5, 9]. Little or no sample preparation is necessary to analyze the fume since it can be placed directly in a diffractometer after collection, provided it has been collected on a suitable substrate that will not interfere with the analysis. This has been a widely used technique in fume studies to date since it provides an easy method of analyzing bulk fume [4, 9, 12, 13].

Previous welding fume studies have also shown that surface compositions of particles may differ somewhat from particle cores by using the surface sensitive technique, X-ray photoelectron spectroscopy (XPS) [4, 9, 15]. Other techniques discussed previously generally analyze the volume of an entire particle but XPS analyzes only approximately 1 to 3 nanometers of the particle surface during an analysis [16]. Surface composition is significant since it is most likely particle surface elements and compounds that interact with the human body as opposed to those in the particle cores. Therefore any fume study should include some method of analyzing particle surface composition.

2 EXPERIMENTAL PROCEDURES

2.1 Fume sampling

Three methods of particle sampling were used to collect welding fume particles during welding with a variety of consumables including AWS E6010, AWS E7018, AWS E308-16, and AWS ER70S-6. The base material used with the E308-16 rod was 6.4 mm thick AISI 304L (UNS S30403). ASTM A36 (UNS K02600) mild steel (6.4 mm thick) was used as a base material for the steel consumables. The composition of the base material and weld deposits are shown in Table 1. A bulk fume collection hood based on the ANSI/AWS F1.2:1999 standard was modified to incorporate a filter medium that exceeds that specified in the standard [17]. A pore size of 0.3 μm was used instead of the 4 μm pore size of the AWS recommended filter. This would ideally trap many of the fine and ultra-fine particles that may pass through the 4 μm filter. The fume collection hood is shown in Figure 1 a).

A thirteen stage electrical low pressure cascade impactor (ELPI) was used to collect fume generated by the different consumables. The rate at which fume was drawn into the impactor was 10 liters min^{-1}. The ELPI was designed for real-time monitoring of aerosol particle size distributions. Using 12 detection channels, the ELPI has the ability to distinguish a size distribution range of 0.03 to 10 μm by sensing electrical currents of charged particles. The operating principle is based on charging, particle inertia, and electrical detection [18]. The fume sampling occurred at a point near the source of fume generation then was drawn through the ELPI where it initially passed through a corona charger. The charger produces a field of ions, which place a positive charge on each of the incoming fume particles. Once charged, the particles enter the impactor column where they are separated by inertial classification according to aerodynamic diameter as they pass through the different stages. As the fume passes through the jet plate of each successive stage, particles larger than a certain dimension are unable to make the sharp turn required to reach the following stage, causing them to impact on the collection substrate directly below the preceding stage as illustrated in Figure 1 b). Each stage has a particular cut-off diameter that determines the particle size that should not pass through to the following stage. The cut-off diameter for each stage is defined as the aerodynamic diameter of particles collected on that stage with an efficiency of 50 % [see Figure 1 c)]. Fume is drawn through the

Table 1 – Composition (wt-%) of base material and weld deposits made during fume collection

Element	ASTM A36 (UNS K02600)	AISI 304L (UNS S30403)	E6010	E7018	E308-16	ER70S-6
C	0.18	0.019	0.15	0.085	0.086	0.12
Mn	0.70	1.46	0.56	0.81	0.95	1.00
Si	0.19	0.29	0.20	0.19	0.61	0.47
P	0.012	0.033	< 0.005	< 0.005	0.019	0.009
S	0.020	0.001	0.020	0.014	0.015	0.015
Ni	0.10	8.34	0.048	0.11	9.13	0.045
Cr	0.064	18.27	0.063	0.15	19.75	0.031
Mo	0.022	0.47	0.018	-	0.22	0.014
Cu	-	0.34	-	-	0.12	0.020

The balance of composition is Fe.
(Compositions measured with mass spectrometry).

a) Fume collection hood, electrode feed system, and rotary positioning system

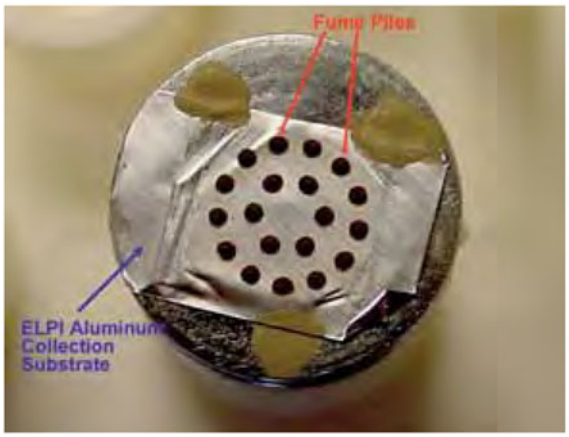

The fume particles piles are clearly evident as the dark spots on the substrate.

b) Aluminium collection substrate from the ELPI mounted on aluminium SEM analysis post

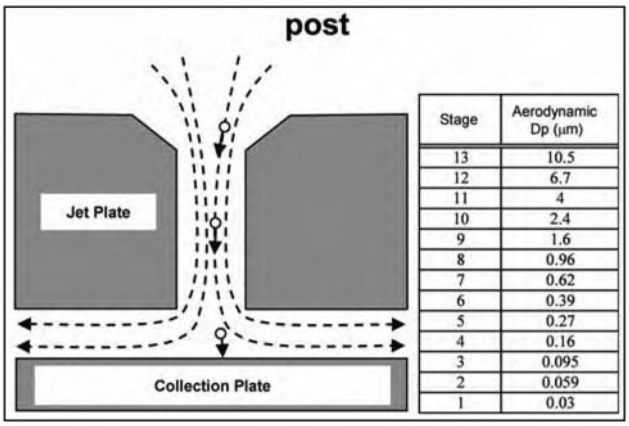

Stage	Aerodynamic Dp (μm)
13	10.5
12	6.7
11	4
10	2.4
9	1.6
8	0.96
7	0.62
6	0.39
5	0.27
4	0.16
3	0.095
2	0.059
1	0.03

c) Schematic of cascade impactor operation and average particle diameters for each stage

Figure 1 [18]

system by means of negative pressure created by an external vacuum pump. Samples collected with the ELPI were analyzed with characterization techniques including SEM, TEM, and XPS.

Additional TEM samples were made by collecting particles on Cu and Au grids with carbon coatings. The Cu grids were used for collection of E6010, E7018, and E308-16 but the presence of a Cu-coating over the ER70S-6 required a different grid material be used so XEDS analysis would not be affected by the substrate. These grids were passed through the fume at different heights above the arc and for different lengths of time during welding. Fume particles deposited on the carbon coatings during immersion in the fume plume.

2.2 XRD

Data were collected using a Scintag XDS-2000 diffractometer equipped with a Cu X-ray tube and an energy-dispersive i-Ge detector. The goniometer was a vertical θ-θ arrangement in a standard Bragg-Brentano geometry. The i-Ge detector energy window was set to detect the CuKα X-rays and reject the CuKß and sample fluorescence such as that from the Fe containing samples. The scans were run from 15° to 70° 2θ at a scan rate of 0.2 to 0.5 degrees per minute with the X-ray source running at 45 kV and 20 mA. Data analysis was performed using MDI Jade software (Version 6.1) and Bruker/Socabim EVA (Version 7.0). Phases were identified by comparison with the ICDD/ICSD 2002 PDF database. An off-axis zero background Si-crystal sample slide was used to hold the fume in the diffractometer. A thin coating of petroleum jelly was applied to the slide to allow the fume to adhere, and the fume filter was pressed onto the slide. The bulk fibreglass filters were pressed onto the slide, causing the fume to stick to the jelly.

2.3 SEM

Three SEM instruments were used for this study. SEM analyses were performed with conventional and high resolution scanning electron microscopes, JEOL FEG-SEM JSM 6330F and JEOL LV-SEM JSM 5900LV, respectively. The conventional SEM has a microanalysis XEDS system, NORAN Voyager equipped with a Si(Li) detector. The third SEM was a high resolution SEM, FEI Sirion, equipped with a Field Emission Gun

(FEG). This SEM has a EDAX microanalysis XEDS system, equipped with a Si(Li) detector. Particle and bulk chemical analysis was performed at accelerating voltages in the range from 10 to 20 kV, and a pole piece to sample distance of 5 mm. For the XEDS analysis, a minimum spectrum collection time of 100 seconds was always used. Monte Carlo electron trajectory simulations were carried out for several fume particle compositions, showing that particle interaction volumes were on the order of 0.3 to 0.5 µm.

2.4 TEM

Transmission electron microscopy (TEM) provides the highest spatial resolution available for determining both the morphology and composition of individual fume particles less than approximately 300 nanometers in diameter. The TEM analyses were performed with a JEOL HRTEM JEM 3010 coupled with chemical micro- and nano-analysis by XEDS, and a NORAN Voyager XEDS collection and analysis system equipped with a Si(Li) detector. A double tilt beryllium sample holder was used for crystallographic analysis and low background chemical analysis. TEM analysis was performed at 300 kV using a large range of magnifications, from 10 000 X to 1 000 000 X. Several techniques, including bright field, dark field, selected area diffraction, nano-beam diffraction and XEDS microanalysis were performed. For the microanalysis, probes of 5 to 25 nm in diameter were used. In order to provide reliable statistics on the spectra collection, 400 second collection times were used. The images and electron diffraction patterns have been recorded on TEM-film as well as digitally using a 1 024 × 1 024 pixel CCD camera. High resolution TEM was also performed on selected core-shell particles. Monte Carlo electron trajectory simulations were carried out for several fume particle compositions measured with TEM-XEDS showing that the incident electron beam had an essentially columnar interaction volume in most particle sizes analyzed with TEM.

2.5 XPS

The XPS system used for this study was a Kratos Ultra Axis XPS and UPS system with depth profiling capabilities using Ar^+ ion etching. Stage 3 ELPI collections were used for the XPS analyses providing an average particle aerodynamic diameter of 0.095 µm. This instrument was equipped with a "sputtering" gun which bombards the surface with argon atoms, thereby removing layers of atoms from the surface revealing the composition of the underlying material. This depth profiling feature of XPS allows both the surface and underlying composition of fume particles to be examined and the valence states of various metallic elements to be determined.

3 RESULTS AND DISCUSSION

3.1 Collection techniques

Welding fume research to date has been inconsistent in that many different techniques have been used to collect and characterize the fume. In a given study only 1 or 2 techniques were used. No study has used the combination of techniques, as presented here, to fully characterize the chemical nature of the welding fume. The major advantage of the study presented in this work is that it utilized state-of-the-art aerosol collection techniques with the ELPI and modified fume hood, and multiple characterization techniques that analyze particle morphology, composition, and surface composition, across the entire particle size range.

3.1.1 Fume hood

Using the fume hood, fume generation rate (FGR) measurements were performed for each of the consumables tested in this study as shown along with their corresponding welding parameters in Table 2. The FGRs ranked from lowest to highest were: E308-16, ER70S-6, E7018, and E6010. Based on results from E308-16 and E6010, increasing heat input resulted in increased FGR.

Table 2 – Fume generation rate measurements and corresponding welding parameters for the SMAW and GMAW consumables

SMAW Consumable	Electrode diameter (mm)	Current	Voltage	Travel speed (mm/s)	Heat input (kJ/mm)	Wire feed speed (mm/s)	FGR (g/min)
E6010 (low heat input)	3.175	93	27.1	4.1	0.62	–	0.387
E6010 (high heat input)	3.175	115	30.8	4.7	0.75	–	0.598
E308-16 (low heat input)	3.175	81	24	4.4	0.44	–	0.091
E308-16 (high heat input)	3.175	115	27	4.6	0.68	–	0.198
E7018	3.175	126	23.8	4.6	0.66	–	0.365
SMAW Consumable	**Electrode diameter (mm)**	**Current**	**Voltage**	**Travel speed (mm/s)**	**Heat input (kJ/mm)**	**Wire feed speed (mm/s)**	**FGR (g/min)**
ER70S-6 (100 % CO2)	1.143	158	20.4	4.4	0.73	71.5	0.207
ER70S-6 (75 % Ar-25 % CO2)	1.143	164	18.1	4.4	0.67	71.1	0.196

3.1.2 ELPI

The ELPI formed the cornerstone of this study. First and foremost it was used to collect and separate particles by aerodynamic diameter into 13 size ranges [Figure 1 c)] and measure the particle number distributions by electrical detection of the particles and mass distribution by weighing collection substrates before and after collection with a precision (accurate to 10^{-5} grams) analytical balance. These measurements were performed for all of the welding consumables as shown in Figure 2 where the percentage of particles measured is plotted versus log of particle aerodynamic diameter. Log scales were used due to the large size variation of fume particles, creating a log-normal distribution. Solid lines indicate number distributions, and dashed lines indicate mass distributions. Error bars indicate one standard deviation of three collections.

The distributions from E6010, E7018, and ER70S-6 showed that the peak *number* of particles was within the ultra-fine particle size range and the E308-16 *number* of particles peaked within the fine particle size range. Further consideration showed that many of the fumes exhibited multi-modal distributions which would be expected in fume formed from multiple formation mechanisms, i.e., nucleation, accumulation, and weld microspatter. The nucleation and accumulation ranges were difficult to distinguish due to the limitations of impactor particle size separation. For example, the aerodynamic diameter of an agglomerate of accumulated particles may be equivalent to a primary particle (condensed from vapour) depending on particle density, which is related to composition, as well as shape and surface smoothness. This caused the large peak in number distributions, encompassing both size ranges. Near the larger sizes within the ELPI separation range the consumables generally exhibited some increase in fume particle concentration as evident by a third mode. This increase was a result of the largest particle sizes, which are formed by microspatter and/or accumulation of many primary particles.

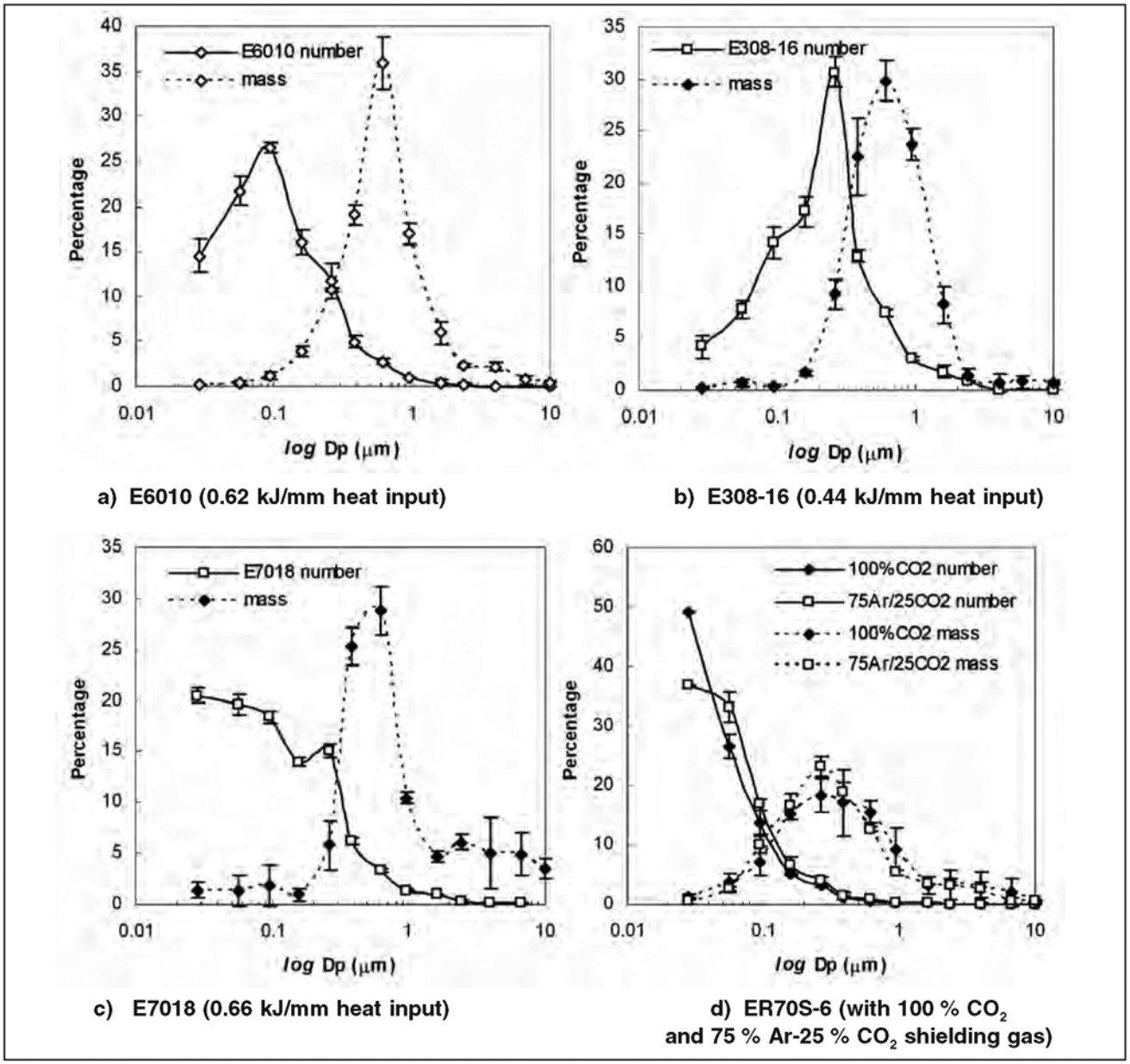

Figure 2 – Number and mass distributions of fume collections

This same reasoning can be applied to explain the behaviour of mass distributions. Similar to the number distributions, multiple modes were often observed in these types of distributions. The nucleation size region typically showed almost no weight at all since these particles make up a very small percentage of total fume mass. The largest mass peaks were usually found in the range of 0.1 µm to 1.0 µm aerodynamic diameter, which represents the range of particle accumulation. A third peak in particle mass was found in the range of approximately 1.0 µm to 10 µm which is the accumulation and spatter range. It has been shown in previous work that mass distributions are usually dominated by particle sizes in the fine and coarse particle regimes [19, 20], which is consistent with these results.

Average number and mass distribution data for the collections performed in this study are provided in Table 3. The number percentage of particles (*N %*) is clearly skewed towards the smaller particle sizes for the different fume collections, whereas mass percentage (*M %*) consists primarily of particles in the accumulation range. E6010, E7018, and ER70S-6 number percentages peaked in the ultra-fine particle range whereas the E308-16 number percentage peaked near the smallest diameters of the fine particle range. Particle mass distributions for all of the consumables was spread over larger particles sizes than the number distributions peaking within the fine particle range.

Statistical analyses are quite simple to perform after distribution data is recorded via the ELPI acquisition system or measured via mass balance. Statistics becomes a powerful tool often used to describe certain aspects of the log-normal distributions of welding fume particles. Calculations were performed on all of the number and mass distributions to obtain geometric mean particle diameter (Equation 1), geometric standard deviation of the distributions (Equation 2), and the percentage of particles lying within n*standard deviations of the geometric mean diameter [10]. Data resulting from these calculations is shown in Table 4. Mean particle diameters were well within the smaller end of the accumulation region down to the nucleation size region. Almost 70 % of GMAW fume particles were within the nucleation size regime though distributions showed evidence of another mode in the accumulation region. Mass distributions are clearly dominated by particles in the accumulation size range. These statistical analyses support the observations made concerning the behaviour of size and mass distributions.

$$\log d_g = \frac{\sum n_i \log d_i}{\sum n_i} \quad (1)$$

$$\log \sigma_g = \left[\frac{\sum n_i (\log d_g - \log d_i)^2}{\sum (n_i) - 1} \right]^{1/2} \quad (2)$$

where

n_i is the number of particles of diameter, d_i.

3.2 Characterization techniques

3.2.1 XRD

An X-ray diffractometer was used to identify bulk phases in the fume from the various consumables. XRD is an excellent technique for bulk analysis since fume can easily be collected on filter media. A Fe_3O_4 type phase with some substitution of Mn for Fe was the primary phase in fumes from each electrode. The substitution of Mn for Fe was evident by peak shifts observed in the diffraction spectra. Shielding gas had little effect on FGR of the GMAW wire but the 100 % CO_2 shielding gas pro-

Table 3 – Size (*N %*) and mass (*M %*) distribution percentages for the different fumes collected

Electrode		E6010				E308-16				E7018		ER70S-6 (100 % CO_2)		ER70S-6 (75 % Ar-25 CO_2)	
Heat input (kJ/mm)		0.62		0.75		0.44		0.68		0.66		0.73		0.67	
Stage	Dp (µm)	N %	M %	N %	M %	N %	M %	N %	M %	N %	M %	N %	M %	N %	M %
1	0.028	14.5	0.2	10.0	0.3	4.2	0.2	1.8	0.3	20.5	1.4	49.2	1.3	36.7	0.6
2	0.056	21.8	0.4	16.0	0.8	7.8	0.7	4.5	0.3	19.6	1.3	26.5	3.6	33.1	2.6
3	0.094	26.6	1.2	24.3	1.1	14.2	0.4	10.3	0.8	18.4	1.8	13.6	7.3	16.8	10.1
4	0.16	16.0	3.9	18.7	4.0	17.2	1.7	15.1	3.3	14.0	1.0	5.3	15.3	6.5	16.4
5	0.26	11.7	10.7	17.2	10.5	30.7	9.2	36.7	13.9	15.1	5.7	3.1	18.4	3.9	23.0
6	0.38	4.9	19.1	7.3	16.2	12.9	22.5	15.5	25.1	6.2	25.1	1.2	17.1	1.5	18.9
7	0.62	2.8	35.8	4.3	29.9	7.4	29.8	8.9	25.3	3.4	28.7	0.6	15.5	0.8	12.7
8	0.95	1.0	17.1	1.5	19.0	3.1	23.7	3.7	20.3	1.4	10.5	0.2	9.2	0.3	5.3
9	1.61	0.5	6.0	0.5	7.9	1.8	8.3	2.5	8.1	1.0	4.7	0.2	3.2	0.2	3.4
10	2.4	0.2	2.3	0.2	4.2	0.8	1.4	1.0	1.3	0.3	6.1	0.1	3.7	0.1	3.2
11	4.0	0.0	2.2	0.0	3.4	0.1	0.8	0.1	0.6	0.2	5.2	0.0	2.9	0.0	2.5
12	6.7	–	0.8	–	2.2	–	0.8	–	0.5	0.1	5.0	–	2.0	–	0.6
13	10.0	–	0.4	–	0.4	–	0.7	–	0.3	–	3.5	–	0.5	–	0.7

Table 4 – Statistical analysis data from ELPI number and mass distributions

Consumable (Heat input)	Geometric mean diameter (µm)	Geometric standard deviation	67 %	95 %
Number Distribution Statistics			**Range (µm)**	**Range (µm)**
E6010 (0.62 kJ/mm)	0.102	1.18	0.087 to 0.120	0.044 to 0.241
E6010 (0.75 kJ/mm)	0.129	1.18	0.109 to 0.152	0.055 to 0.304
E308-16 (0.44 kJ/mm)	0.206	1.18	0.175 to 0.243	0.088 to 0.486
E308-16 (0.68 kJ/mm)	0.253	1.15	0.220 to 0.290	0.110 to 0.581
E7018 (0.66 kJ/mm)	0.105	1.25	0.084 to 0.131	0.042 to 0.263
ER70S-6 100 % CO_2 (0.73 kJ/mm)	0.049	2.06	0.024 to 0.103	0.012 to 0.206
ER70S-6 75 % Ar – 25 % CO_2 (0.67 kJ/mm)	0.058	2.10	0.027 to 0.121	0.014 to 0.243
Mass distribution statistics			**Range (µm)**	**Range (µm)**
E6010 (0.62 kJ/mm)	0.592	1.13	0.525 to 0.668	0.262 to 1.335
E6010 (0.75 kJ/mm)	0.662	1.17	0.564 to 0.777	0.282 to 1.553
E308-16 (0.44 kJ/mm)	0.625	1.11	0.561 to 0.695	0.281 to 1.391
E308-16 (0.68 kJ/mm)	0.557	1.11	0.501 to 0.619	0.251 to 1.237
E7018 (0.66 kJ/mm)	0.747	1.32	0.566 to 0.984	0.283 to 1.969
ER70S-6 100 % CO_2 (0.73 kJ/mm)	0.386	3.00	0.129 to 1.156	0.064 to 2.313
ER70S-6 75 % Ar – 25 % CO_2 (0.67 kJ/mm)	0.338	2.71	0.125 to 0.916	0.062 to 1.833

duced higher concentrations of FeO in the bulk fume than the 75 % Ar-25 % CO_2 because of the higher oxygen potential in the shielding atmosphere. The other compounds were formed from constituents used in the flux from each of the welding electrodes. The E308-16 also showed strong peaks for a $K_2(Cr,Mn,Fe)O_4$ compound. Cr, Mn, and Fe in this form would have an oxidation state of (VI). Cr(VI) is dependent on the presence of K in the fume since the formation of the $K_2(M)O_4$ phase is necessary for a +6 metal oxidation state. The element potassium (K) is a common addition in basic electrode coatings. Several other peaks were identified from flux additions as well, primarily NaF and CaF_2. Each of the compounds identified and their relative strengths are shown in Table 5.

3.2.2 SEM

Particle morphology is important to consider because it can change the aerodynamic behaviour of the particles and affects the total surface area of the particle that may eventually come into contact with human tissues. Some agglomerates while large in size, may have a lesser aerodynamic diameter than a much smaller individual spherical particle because their aerodynamic velocity in a flowing air stream is lower than that of a spherical particle. An analogy of this is dropping a dense spherical object and feather of a much larger size; though the feather may have a greater mass, the spherical object will impact the ground first. Examinations of many of the lower ELPI stages (smaller aerodynamic cut-off diameters) showed higher concentrations of agglomerates than the upper stages. Figure 3 shows a schematic of the particle morphologies that were observed and representative secondary electron micrographs of several of the fumes collected on ELPI stages. Irregular particles were observed with low frequency on ELPI stages, and their total number may be considered a small fraction of total number of particles.

Bulk chemical analyses using SEM-XEDS were performed on the ELPI stages to determine average compositions versus aerodynamic particle diameter. Some variation in composition was measured as a function of aerodynamic diameter as shown in plots of element atomic percentage versus the particle diameters (see Figure 4) though compositions appear fairly uniform in each size range (i.e., ultra-fine, fine, and coarse) for

Table 5 – Bulk fume phases identified with XRD and their relative intensities to each other

SMAW Consumable	Fe_3O_4	$K_2(M)O_4$	FeO	Fe	NaF	CaF_2
E6010	Strong	–	–	–	–	–
E308-16	Strong	Medium	–	–	Weak	–
E7018	Strong	–	–	–	Medium	Weak
GMAW Consumable	**Fe_3O_4**	**$K_2(M)O_4$**	**FeO**	**Fe**	**NaF**	**CaF_2**
ER70S-6 (100 % CO_2)	Strong	–	Weak	Medium	–	–
ER70S-6 (75 % Ar-25 % CO_2)	Medium	–	Weak	Strong	–	–
Diffraction peak intensity is ranked from strong (highest) to weak (lowest)						

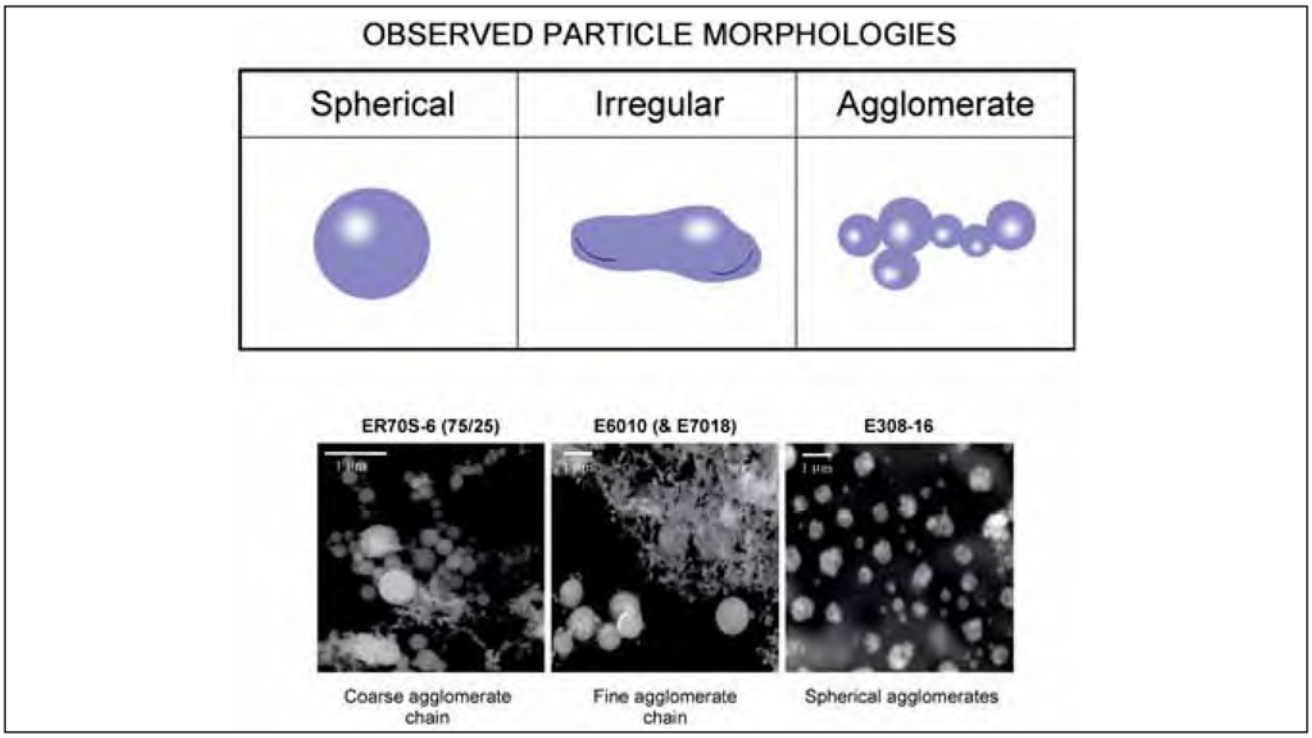

Figure 3 – Schematic of fume particle morphologies and representative secondary electron micrographs showing some typical individual spherical particles and particle agglomerations

most fumes with the exception of E6010. This data is not completely representative of fume composition since XEDS cannot be used to accurately report atomic numbers below Z = 11 (Na), which discounts both O and F from all of the analyses. Considering that most of the metallic constituents are found in the form of oxides such as Fe_3O_4 (as shown by XRD) and that fluoride compounds are a common addition to many of the fluxes, distribution of composition across the particle size range is only an estimate of actual composition.

Table 6 shows average bulk compositions in atomic percent from the ultrafine (UF), fine (F), and coarse (C) particle size regions for fume generated by each consumable. Note that ratios of Mn/Fe and (Mn+Cr)/Fe (for the stainless steel fume) are shown in this table. These ratios give a reasonable estimate of the fraction of substitution for Mn and Cr in the Fe_3O_4 and $K_2(M)O_4$ compounds identified with XRD. The ratio of substitution of Mn for Fe in the mild steel electrode fumes averaged approximately 0.13 or $(0.87Fe,0.13Mn)_3O_4$. The fraction of Mn substitution in the stainless steel fume is considerably higher at approximately 0.66 or $(0.34Fe, 0.66Mn)_3O_4$ though it is likely that some Cr is also present in the Fe_3O_4-type crystal structure.

Considering results from the composition distribution of fume generated by ER70S-6 welding wire, the general

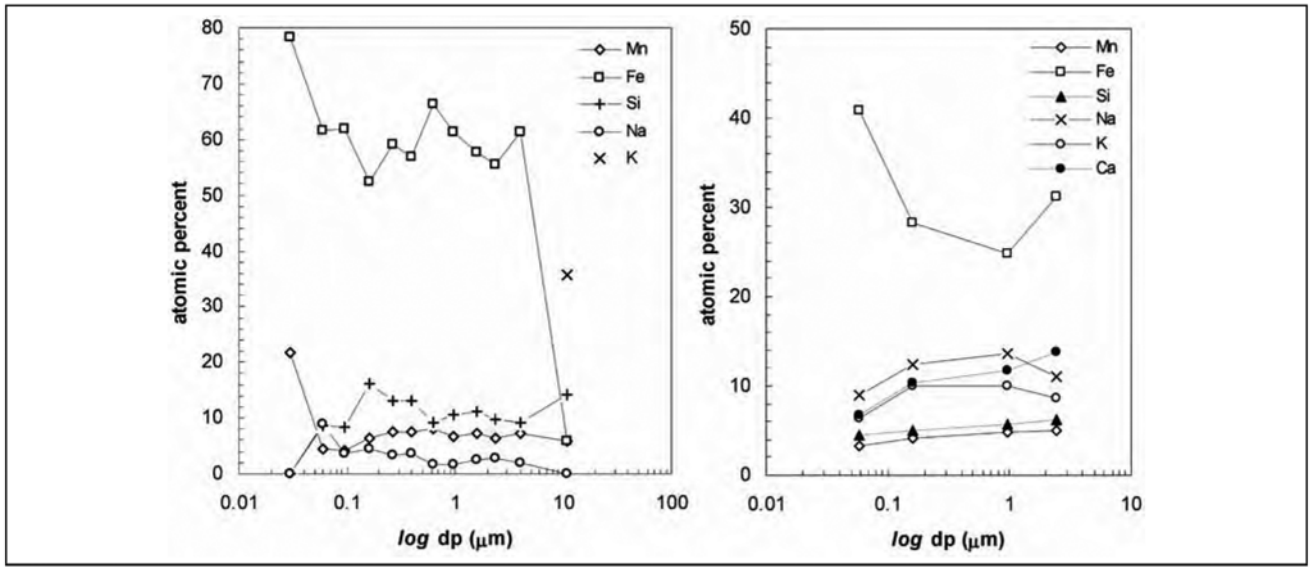

Figure 4 – Bulk ELPI stage compositions of welding fume as measured with SEM-XEDS

Table 6 – Average ELPI stage compositions (atomic percent) for the different welding consumables and typical particle morphologies

Electrode	E6010			E308-16			E7018			ER70S-6 (100 % CO_2)			ER70S-6 (75 % Ar- 25 % CO_2)		
Size range	UF	F	C	UF	F	C	UF	F	C	UF	F	C	UF	F	C
Element	At-%			At-%			At-%			At-%			At-%		
Mn-K	11.6	8.7	8.7	5.7	6.8	5.4	4.4	6.0	6.3	10.5	12.8	7.7	9.9	10.6	6.3
O-K	*	*	*	*	*	*	*	*	*	*	*	*	*	*	*
Fe-K	76.7	71.6	58.1	16.1	6.8	8.5	55.0	35.2	38.6	75.9	73.8	85.6	71.6	74.2	87.0
Cr-K	–	–	–	13.0	5.7	8.5	–	–	–	–	–	–	–	–	–
Si-K	6.5	15.1	14.2	9.4	13.9	17.4	6.0	7.1	7.7	12.4	13.2	4.1	17.3	15.0	6.7
Na-K	4.8	3.6	2.3	1.9	1.9	1.8	12.1	17.3	13.7	–	–	–	–	–	–
Ti-K	–	0.5	2.1	1.9	2.6	2.9	–	0.6	1.3	–	–	–	–	–	–
Mg-K	–	0.4	–	–	0.2	–	–	0.1	0.7	–	–	–	–	–	–
S-K	0.2	–	0.2	–	0.1	3.2	0.8	0.2	–	–	–	–	–	–	–
Cl-K	0.2	–	0.3	1.9	0.9	0.8	0.4	0.3	0.2	–	–	–	–	–	–
K-K	–	–	12.5	50.1	60.2	49.6	8.6	13.3	10.6	–	–	–	–	–	–
F-K	–	–	–	–	–	–	*	*	*	–	–	–	–	–	–
Ca-K	–	–	0.5	0.1	1.0	2.0	9.1	14.6	17.1	–	–	–	–	–	–
Zn-K	–	–	–	–	–	–	3.8	5.4	3.8	–	–	–	–	–	–
Cu-K	–	–	–	–	–	–	–	–	–	1.2	0.2	2.6	1.2	0.2	0.0
Mn/Fe	0.15	0.12	0.15	0.36	1.00	0.63	0.08	0.17	0.16	0.14	0.17	0.09	0.14	0.14	0.07
(Mn+Cr)/Fe	–	–	–	1.16	1.83	1.64	–	–	–	–	–	–	–	–	–
Observed particle morphology	individual spherical, agglomerated, irregular			individual spherical, spherical agglomerated, agglomerated, irregular			individual spherical, agglomerated, irregular			Individual spherical, agglomerated			Individual spherical, agglomerated		

Average composition calculated for each size range: UF (< 100nm), F (100nm – 1µm), C (> 2.5µm).
* Indicates O-K and/or F-K present.

trend of composition change can be described by the following explanations given in previous studies [4, 9]. Coarse particles are most likely formed by mechanical means such as spatter, thus higher Fe concentrations (over 90-wt % Fe) were found in large particles since the composition will be close to that of the deposited filler metal. Fe decreased and Si and Mn increased in composition in the smaller particles since Si and Mn are more volatile than Fe. A similar argument can be used to explain trends with the SMAW electrodes; however, the complexity of the SMAW fume due to additional flux elements may change some of the trends. Ultra-fine particles collected from E6010 fume were enriched in Fe and Mn; E7018 ultra-fine particles were also enriched in Fe. The smallest particles in E308-16 fume showed increases in Fe and Cr as compared to the larger particles as well as a decrease in Si. Individual particle analyses with XEDS generally coincided with compositions measured for the bulk fume of similar sizes on the ELPI.

It is important to note that the composition of each impactor stage does not accurately represent the bulk fume composition, since a bulk measurement would include particles across all size ranges; therefore average compositions of the three aerosol size ranges were calculated from SEM-XEDS measurements made on ELPI stages as shown in Table 6. It should also be noted that the average composition of agglomerates and accumulated particles, which consist of multiple primary particles (formed from vapour), will not reflect the composition of the ultra-fine particles but rather an average of those particle sizes. This is due to the fact that ultra-fine particles collide with other particles and sinter or coalesce to form an agglomerate or accumulated particle that has an average composition of the primary particles. The composition of the primary particles is based on the vapour from which they condensed, and it is possible that the vapour may vary in composition (and volatility) in different regions of a welding arc. It has been shown in previous TEM-XEDS work of ultra-fine particles that chemical variation is strongly dependent on the size of ultra-fines [4].

3.2.3 TEM

Individual ultra-fine particles were analyzed and imaged with TEM. Selected area diffraction (SAD) studies showed that most particles were crystalline in nature with the exception of some amorphous particles, which were usually on the order of several nanometers in diameter. Fe_3O_4-type crystal structures were observed with the highest frequency for particles generated by all con-

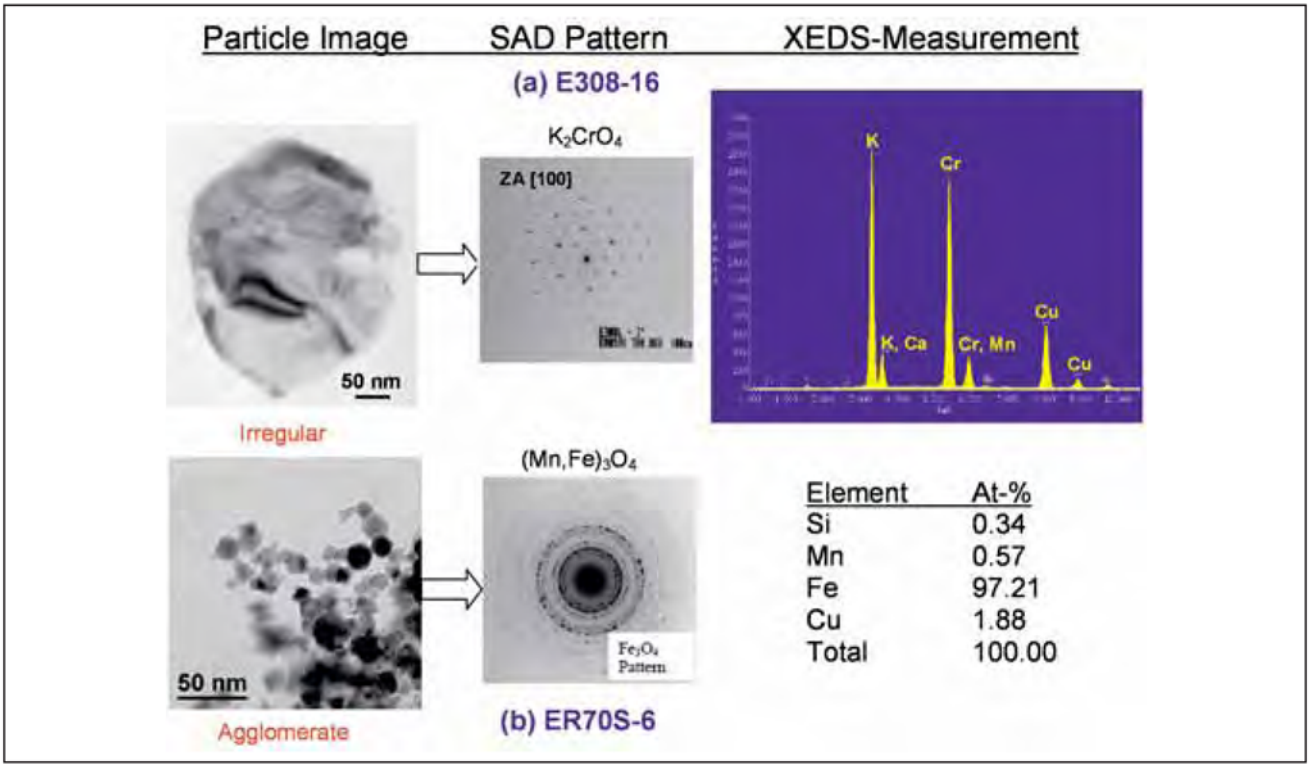

Figure 5 – TEM analyses of ultrafine fume particles

sumables, whereas the small amorphous particles were usually highly enriched in Si. The Fe_3O_4 crystal structure was usually accompanied by slight shifts in diffraction patterns caused by substitution of Mn and other elements (dependent on electrode composition, for example, 308-16 had Cr and Mn) for Fe. XEDS confirmed that ultra-fine particles were generally Fe-oxides with additional alloying of Si and Mn. Oxygen was also observed with high intensity in most of the XEDS spectra measurements but was not quantified due to large errors that would be inherent with doing so.

Typical TEM analyses included imaging a particle or agglomerate, followed by obtaining a SAD pattern and chemical composition with XEDS. A representative example is shown in Figure 5 where (a) E308-16 and (b) ER70S-6 100 % CO_2 particles were analyzed. Peaks for Cu in XEDS measurements are a result of using Cu TEM grids to collect fume samples, with the exception of the ER70S-6 which was collected on Au grids. This was done since there was a Cu-coating on the ER70S-6 wire, which ultimately ended up in the fume after welding.

3.2.4 XPS

XPS impinges X-rays onto the fume sample surface, which causes emission of photoelectrons from atoms on or near the sample surface. Each electron is associated with a specific electron orbital of the element from which it was emitted. The signal intensity measured for each electron orbital (i.e., 1s, 2p) is proportional to the atomic percentage of the element from which it was emitted. The measured intensity from each orbital was normalized by the orbital with the strongest intensity of ELPI Stage 3 (Dp = 0.094 µm) for the various consumables as displayed in Table 7. Slight shifts of these photoelectron peaks correspond to certain compounds that are present in the sample. The most probable compounds (or elements) for the observed peak shifts are also shown in Table 7. Since these compounds match those found with XRD and SAD, there is high certainty that the results from XPS are a fairly accurate estimate of surface composition of the bulk fume collected on the ELPI stages. Peak shifts of the Fe 2p and O 1s peaks corresponded to Fe_3O_4 type compounds. Mn appeared in the +2 and +3 oxidation state, which would be consistent with a substitution of Mn for Fe in Fe_3O_4. Peaks corresponding to the Cr +6 oxidation state were not specifically found in the E308-16 fume analysis. Other compounds such as SiO_2, NaF, and KCl were detected in the fumes and their presence was dependent on flux composition of the consumable.

Two limitations of using XPS to examine particle composition are poor spatial resolution inherent to the technique, and the difficulty in determining which particle surface(s) are actually being analyzed since the pile of particles deposited on the ELPI collection substrate are three dimensional in nature. These limitations must be considered when analyzing results from this technique.

3.2.5 Core-shell particles

An interesting feature of many fume particles that was observed using TEM and XPS was the presence of a core-shell structure. This type of particle forms when multiple compounds are introduced into the welding arc from processes that include flux (FCAW, SMAW) or because of alloying in the filler metal (GMAW). Metallic-oxide particles were found with coatings of lighter atomic number elements. These particles are thought to be

Table 7 – XPS characteristic peak intensities and likely surface elements and compounds

SMAW consumable	Mn 2p	Fe 2p	Cr 2p	Si 2p	Ca 2p	Na 1s	O 1s	F 1d	K 2p	Cl 2p
E6010 surface	1.2	10.9	–	0.9	–	28.5	57.7	0.8	–	–
	Likely compounds and elements: (Fe,Mn)3O4, SiO2, Na, F									
E6010 sub-surface	4.0	30.5	–	2.2	–	20.7	42.5	0.0	–	–
	Likely compounds and elements: (Fe,Mn)3O4, SiO2, Na, F									
E308-16 surface	0.2	1.1	0.2	0.2	–	1.0	7.8	86.1	3.4	0.1
	Likely compounds and elements: (Fe,Mn)3O4, Cr, SiO2, NaCl, NaF, KCl, KF									
E308-16 sub-surface	1.9	6.4	2.5	3.4	–	12.8	28.4	33.8	10.6	0.1
	Likely compounds: (Fe,Mn)3O4, (Na,K)2CrO4, SiO2, NaF, KF									
E7018 surface	–	8.6	–	0.4	10.2	9.3	39.5	22.1	9.8	–
	Likely compounds: Fe3O4, NaF, KF, CaF2, CaCO									
E7018 sub-surface	2.5	26.0	–	3.5	6.3	10.4	23.9	21.6	5.8	–
	Likely compounds: (Mn,Fe)3O4, NaF, KF, SiO2, CaF2, CaCO									
GMAW consumable	**Mn 2p**	**Fe 2p**	**Cr 2p**	**Si 2p**	**Ca 2p**	**Na 1s**	**O 1s**	**F 1s**	**K 2p**	**Cl 2p**
ER70S-6 (CO_2) surface	3.1	14.9	–	0.6	–	–	78.4	3.0	–	–
	Likely compounds and elements: (Fe,Mn)O, (Fe,Mn)3O4, F									
ER70S-6 (CO_2) sub-surface	4.5	48.8	–	4.7	–	–	42.0	–	–	–
	Likely compounds and elements: Fe, (Fe,Mn)O, (Fe,Mn)3O4, SiO2									
ER70S-6 (75 % Ar-25 % CO_2) surface	4.8	20.6	–	1.1	–	–	71.5	2.0	–	–
	Likely compounds and elements: (Fe,Mn)O, (Fe,Mn)3O4, F									
ER70S-6 (75 % Ar-25 % CO_2) sub-surface	20.7	43.1	–	1.5	–	–	34.6	–	–	–
	Likely compounds and elements: Fe, (Fe,Mn)O, (Fe,Mn)3O4, SiO2									
Intensity values are normalized area intensity: N = (I / Io)* 100										

formed by varying condensation temperatures of the elements within the fume, as well is immiscibility of the different phases, namely Si-oxide and magnetite [4, 9, 14]. One important thing that should be mentioned is that particle surface chemistry is potentially of great importance because surfaces are most likely where the particles interact with human tissues.

A summary of the types of core-shell particles that were observed is presented in Table 8. Particle cores were generally metal-oxides consisting of $(Fe,Mn)_3O_4$ type structure in the mild steel and hardfacing electrodes and $K_2(Cr,Mn,Fe)O_4$ in the stainless electrode. The shell coatings consisted of elements and compounds found in the flux for the flux-based processes such as SiO, NaF, and CaF_2. Several GMAW particles were also found to have a thin amorphous shell of SiO or SiO_2, though the frequency of occurrence of those particles was much lower than processes utilizing flux. A high Mn flux cored arc welding consumable was also included in some of the analysis work.

TEM is ideal for imaging core-shell particle structures since particle shells generally diffract the incident beam much less than their crystalline cores due to the amorphous nature of silicon-oxide. This results in high contrast between the core and shell. A typical example of a core shell particle analysis is included in Figure 6. Figure 6 a) shows the structure of an agglomerate consisting of several of these core-shell particles that have sintered together. The corresponding diffraction pattern (found with selected area diffraction) shows a Fe_3O_4 type structure. Two XEDS spot analysis locations are also indicated:

Table 8 – Summary of core-shell particle phases observed with XPS and TEM

	Core type		Shell type		
SMAW Consumable	$(Fe,Mn)_3O_4$	$K_2(M)O_4$	SiO/SiO_2	NaF	CaF_2
E6010	X		X	X	
E308-16	X	X	X		
E7018	X				X
GMAW Consumable	$(Fe,Mn)_3O_4$	$K_2(M)O_4$	SiO/SiO_2	NaF	CaF_2
ER70S-6 (100 % CO_2)	X		X		
ER70S-6 (75 % Ar-2 5 % CO_2)	X				
FCAW Consumable	$(Fe,Mn)_3O_4$	$K_2(M)O_4$	SiO/SiO_2	NaF	CaF_2
High-Mn Hardfacing	X				X

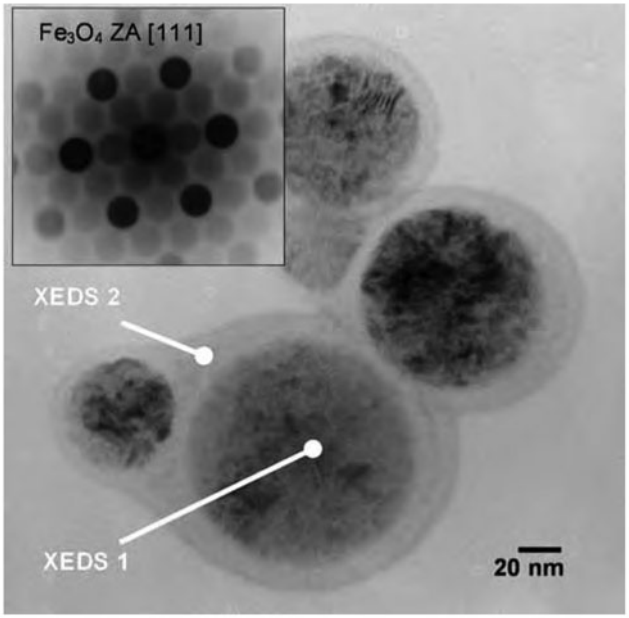

a) TEM image of agglomerate with corresponding SAD pattern and EDS spot analysis locations

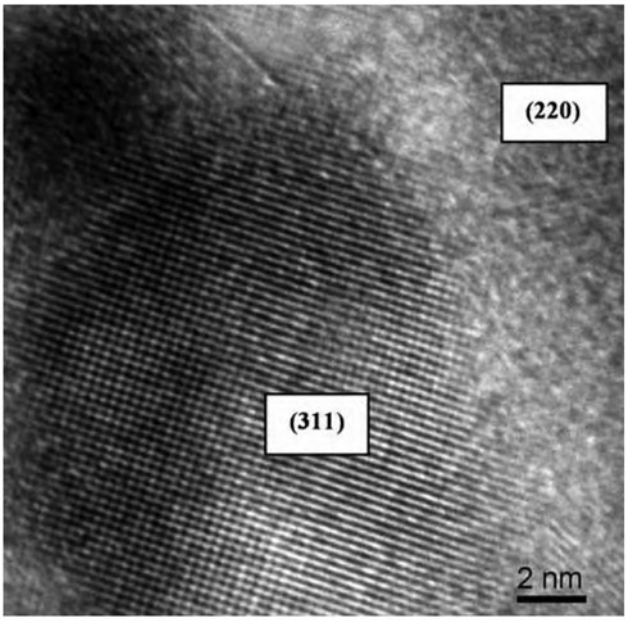

b) High resolution TEM image showing Fe_3O_4 crystal structure along (311) and (220) planes of a submicron sized particle

Figure 6

– **XEDS1**, which measured the core composition, revealed high concentrations of Mn and Fe, whereas,
– **XEDS2**, which measured the shell composition, contained mostly Si and O.

Silicon-oxide and calcium-fluoride compounds were the most common shell constituents. Figure 6 b) shows the crystalline structure of a Fe_3O_4-type particle core.

TEM is also an excellent technique for probing the composition of these core-shell particles since the beam diameter of the TEM can be set to sizes as narrow as 10 nm in diameter. The interaction volume of the beam with the particle of interest generates X-rays from a narrow cylindrical cross-section of the particle (shown with Monte Carlo simulations to be approximately the size of the incident electron beam), thus allowing for fairly accurate composition profiles to be measured. Several of these profiles were measured for particles generated by E6010 and a high-Mn hardfacing consumable.

Typical particle composition profiles for each type is shown in Figure 7 where the core composition is on the

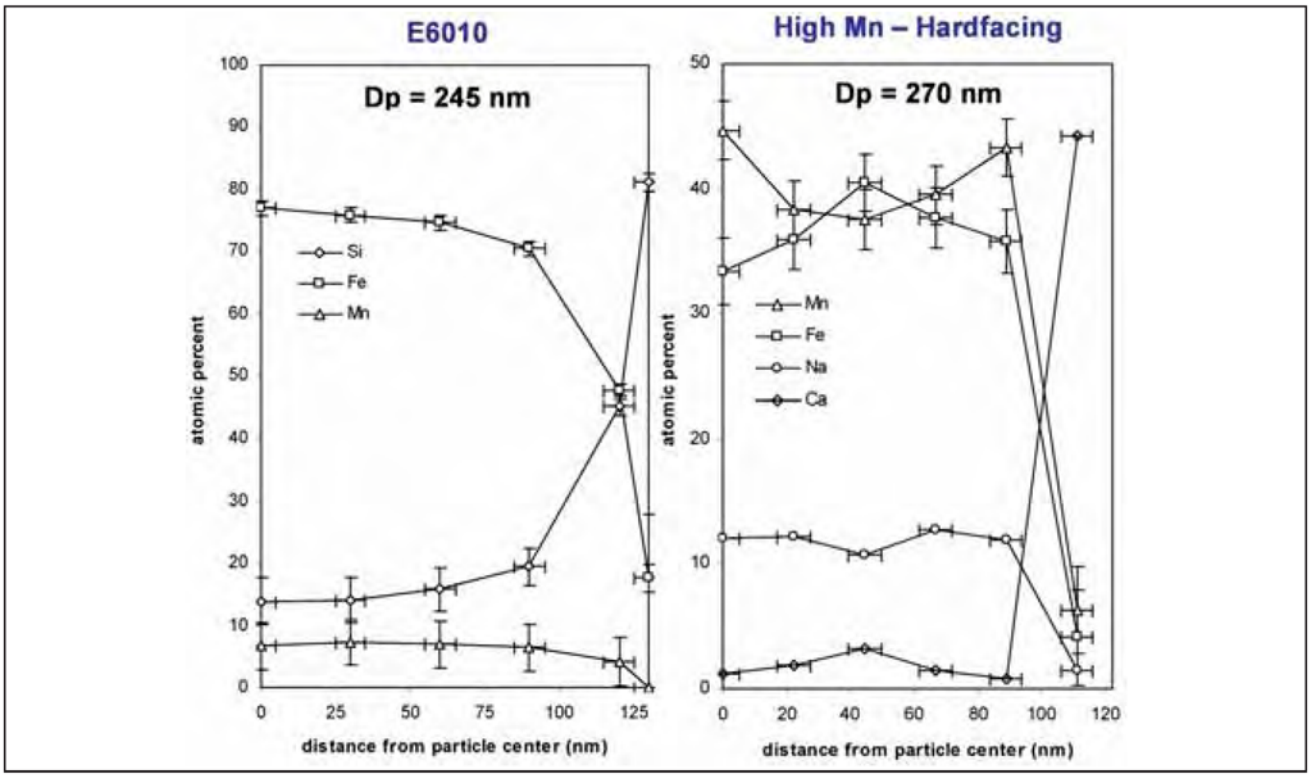

Figure 7 – Core-shell particle composition profiles measured with TEM-XEDS

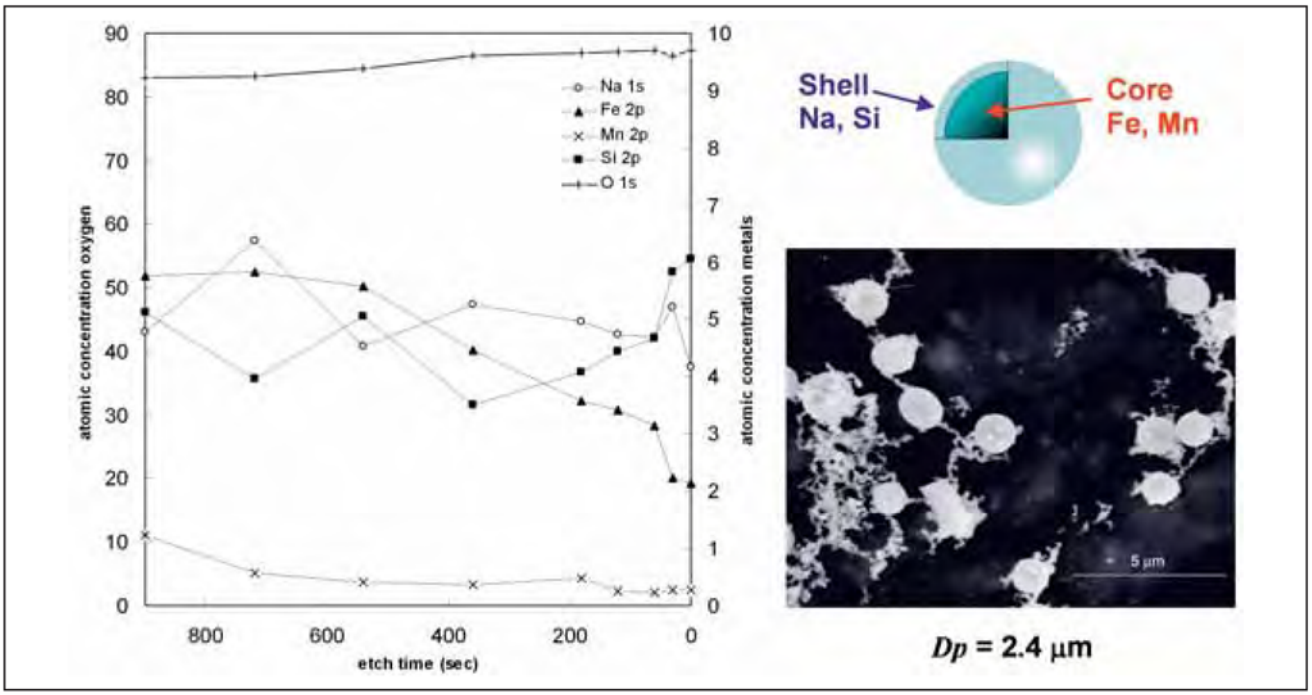

Figure 8 – XPS depth profiling analysis of E6010 fume collection from Stage 10 of ELPI

left side of the figures and the shell composition is displayed on the right side. The E6010 particle composition profile shows 80 at-% Si in the shell, which decreases to approximately 15 at-% in the core. Fe and Mn both increase from 17 to 78 at-% and 0 to 7 at-% respectively in the transition from shell composition to core composition. The hardfacing fume particle composition profile has 45 at-% Ca in the shell which decreases to less than 5 at-% in the core. Large increases are seen in at-% of Mn, Fe, and Na in the transition from shell to particle core. Horizontal error bars indicate approximate beam width of 10 nm and vertical error bars indicate standard error of the measurements. These measurements do not take into account corrections for the beam passing through a portion of the shell coating before measuring core composition, though general trends are the same as what would be expected if corrections were made.

XPS is useful for examining the core-shell phenomenon since it has the capability to provide depth profile information with Ar^+ ion etching. Figure 8 displays results from a depth profiling analysis of E6010 particles collected on Stage 10 of the ELPI. Particle shell composition is represented at zero seconds etch time (right side). By using cycles of subsequent etching and chemical analysis, composition depth profiles were obtained. These showed a trend of decreasing Si and O as well as increasing concentrations of Fe and Mn as etch time increases. The proposed particle model is shown in the Figure along with a secondary electron SEM image representing approximate particle sizes in this analysis. A good correlation was found between TEM-EDS and XPS depth profiling for the E6010 core shell particles in that both had higher silicon concentrations in the shells and higher iron concentrations in core compositions.

4 SUMMARY

Advancing the understanding of welding fume particle size, morphology, and chemistry is of enormous importance since fume is a potential risk in the welding industry. This study used state of the art collection and characterization methods to expand the current knowledge of welding fume and to provide insight into particle size, morphology, and composition. Multiple disciplines were incorporated into this study including: welding physics (fume formation mechanism), aerosol science (important for performing collection and understanding particle mobility), and materials science and chemistry (identify morphology, phases, and chemistry of particles).

The use of an electrical low pressure impactor (ELPI) was an essential tool in this study since it measured size and mass distributions of the different fume collections and provided a method of segregating the fume particles by aerodynamic diameter, thereby allowing them to be analyzed separately from one another. This instrument showed that the number of fume particles was most frequent within the fine and ultra-fine particle ranges, but the highest concentration of mass was in the larger end of the fine particle range. The bulk fume collection system provided fume generation rates and samples for XRD analyses, which showed that the most predominate phase measured in each fume was a Fe_3O_4-type compound with some substitution of other metals such as Mn and Cr for the Fe in the oxide matrix. This substitution was dependent on consumable composition, i.e., mild steel, stainless steel.

SEM and TEM imaging of fume particles showed three particle morphologies with agglomerates being the most frequent type, followed by individual spherical particles, and irregular particles respectively. TEM and XPS revealed the presence of a core-shell structure in many

of the particles, which suggests that surface composition of can be quite different from the bulk compositions.

Results obtained from the different characterization methods were complimentary and validated one another. Therefore it is recommended that future work includes multiple techniques to obtain a better overall understanding of the nature of fume size, morphology, and composition, as well as their relation to each other.

ACKNOWLEDGMENTS

The author would like to acknowledge his academic advisor Prof. John C. Lippold as well as Prof. David W. Dickinson of The Ohio State University, and Dr. Antonio Ramirez of the Brazilian Synchrotron Light Laboratory for their support in the completion of this study. Funding for this project was provided by D&L Welding Fume Analysis LLC representing a consortium of past and current consumable manufacturers.

REFERENCES

[1] Welding Handbook, Vol. 1 8th Edition, American Welding Society, 1987, Miami, FL.

[2] Castner H.R., Null C.L.: Chromium, nickel and manganese in shipyard welding fumes, Welding Journal, 1998, 77, 6, pp. 223-s-231-s.

[3] Zimmer A.T.: The influence of metallurgy on the formation of welding aerosols, J. Environ. Monit, 2002, 4, pp. 628-632.

[4] Jenkins N.T.: Chemistry of airborne particles from metallurgical processing, Ph.D. Dissertation: Materials Science and Engineering, Massachusetts Institute of Technology, Cambridge, MA, 2003.

[5] Jenkins N.T., Eager T.W.: Chemical analysis of welding fume particles, Welding Journal, 2005, 84, 6, pp. 87-s-93-s.

[6] Environmental Protection Agency, Basic concepts in environmental sciences, 2005. http://www.epa.gov/eogapti1/home/index.htm.

[7] Antonini J.M., Krishna Murthy G.G., Rogers R.A., Albert R., Eager T.W., Ulrich G.D., Brian J.D.: How welding fumes affect the welder, Welding Journal, 77, 10, pp. 55-99.

[8] Friedlander S.K.: Smoke, dust, and haze: Fundamentals of aerosol behavior, New York, New York, John Wiley & Sons,1977.

[9] Voitkevic V.: Welding fumes: Formation, properties, and biological effects, Cambridge, England, Abington Publishing, 1995.

[10] Reist, Parker C.: Introduction to aerosol science, New York, New York: Macmillan Publishing Company, 1984.

[11] Newbury D.E., Joy D.C., Echlin P., Fiori C.E., Goldstein J.I. Eds., Advanced Scanning Electron Microscopy and X-ray Microanalysis, New York, New York: Plenum Press, 1986.

[12] Spurny K.R.: Analytical chemistry of aerosols, Boca Raton, Fl.: Lewis Publishers, ed. 1999.

[13] Characterization of Arc Welding Fume, American Welding Society, 1983, Miami, FL.

[14] Ehrman S.H., Friedlander S.K., Zachariah M.R.: Phase segregation in binary SiO2/TiO2 and SiO2/Fe2O3 nanoparticle aerosols formed in a premixed flame, Journal of Materials Research, 1999, 14, 12, pp. 4551-4561.

[15] Tandon R.K., Payling R., Chenhall B.E., Crisp P.T., Ellis J., Baker R.S.: Application of X-ray photoelectron spectroscopy to the analysis of stainless-steel welding aerosols, Applications of Surface Science, 1985, 20, 4, pp. 527-537.

[16] Smith G.C.: Surface analysis by electron spectroscopy, New York, New York: Plenum Press, 1994.

[17] Laboratory method for measuring fume generation rates and total fume emission of welding and allied processes, American Welding Society, 1999, Miami, FL.

[18] ELPI Users Manual, Dekati Ltd, Tampere, Finland.

[19] Sferlazza S.J., Beckett W.S.: The respiratory health of welders, Am Rev Respir Dis, 1991, Vol. 143, pp. 1134-1148.

[20] Jenkins N.T., Pierce W.M.-G., Eagar T.W.: Particle size distribution of gas metal and flux cored arc welding fumes, Welding Journal, 2005, 84,10, pp. 156-s-163-s.